Priegnitz, M., Thaler, J., Spangenberg, E., Schicks, J., Schrötter, J., Abendroth, S. (2015): Characterizing electrical properties and permeability changes of hydrate bearing sediments using ERT data. - *Geophysical Journal International*, *202*, 3, p. 1599-1612.

DOI: http://doi.org/10.1093/gji/ggv245

Geophysical Journal International

Geophys. J. Int. (2015) **202,** 1599–1612
GJI Marine geosciences and applied geophysics

doi: 10.1093/gji/ggv245

Characterizing electrical properties and permeability changes of hydrate bearing sediments using ERT data

Mike Priegnitz, Jan Thaler, Erik Spangenberg, Judith M. Schicks, Jörg Schrötter and Sven Abendroth

Helmholtz Centre Potsdam, GFZ German Research Centre for Geosciences, Potsdam, Germany. E-mail: mikep@gfz-potsdam.de

Accepted 2015 June 5. Received 2015 June 5; in original form 2015 March 9

SUMMARY

A LArge Reservoir Simulator (LARS) was equipped with an electrical resistivity tomography (ERT) array to monitor hydrate formation and dissociation experiments. During two hydrate formation experiments reaching 90 per cent bulk hydrate saturation, frequent measurements of the electrical properties within the sediment sample were performed. Subsequently, several common mixing rules, including two different interpretations of Archie's law, were tested to convert the obtained distribution of the electrical resistivity into the spatial distribution of local hydrate saturation. It turned out that the best results estimating values of local hydrate saturation were obtained using the Archie$_{var-phi}$ approach where the increasing hydrate phase is interpreted as part of the sediment grain framework reducing the sample's porosity. These values of local hydrate saturation were used to determine local permeabilities by applying the Carman-Kozeny relation. The formed hydrates were dissociated via depressurization. The decomposition onset as well as areas featuring hydrates and free gas were inferred from the ERT results. Supplemental consideration of temperature and pressure data granted information on discrete areas of hydrate dissociation.

Key words: Tomography; Electrical properties; Gas and hydrate systems; Permeability and porosity.

1 INTRODUCTION

Gas hydrates are ice-like crystalline solids composed of a 3-D network of water molecules enclosing small (<1 nm) guest molecules (Von Stackelberg *et al.* 1947). Naturally occurring gas hydrates predominantly contain methane (CH_4) as guest molecules, however, higher hydrocarbons and mixed hydrates can be found as well (Milkov *et al.* 2005). Since hydrates are stable wherever sufficient amounts of water, hydrate forming gas, elevated pressure, and low temperatures are present, natural gas hydrates occur at active and passive continental margins, permafrost areas and deep inland seas (Sloan & Koh 2008). Global estimates of methane encapsulated in gas hydrates vary by several orders of magnitude. Whereas Kvenvolden and Grantz (Kvenvolden & Grantz 1990) assumed 1×10^{15} m^3 of CH_4, Klauda & Sandler (2005) estimated that there is as much as 1.2×10^{17} m^3 of methane gas globally bound in gas hydrates. Thus, gas hydrate reservoirs have become of great interest during the last decades, as the amounts of hydrate-bonded carbon are considered to be a potential energy resource as well as a source of greenhouse gases.

Recent efforts aim at conducting field tests to produce methane from hydrate bearing sediments. Generally, gas hydrates can be decomposed by disturbing their thermal equilibrium (heating), mechanical equilibrium (depressurization) or chemical equilibrium (e.g. by injecting CO_2). All of these production techniques have been successfully tested on a field scale: in the winter of 2001/2002 the first ever gas production test directly from hydrate bearing sediments was carried out via thermal stimulation by injecting hot fluid in the hydrate bearing sediment layers at the Mallik test site in the Mackenzie Delta, Canada (e.g. Dallimore & Collett 2005). Later, the decomposition of hydrates via depressurization was carried out at the Mallik test site in 2007/2008 (e.g. Wright *et al.* 2011) and in the Nankai Trough, Japan in 2013 (Yamamoto 2014). The applicability of methane production via CO_2–CH_4 exchange was tested in 2012 at the Alaska North Slope, known as Ignik Sikumi #1 Gas Hydrate Field Trial (Lee & White 2014). Regardless of the decomposition technique, a proper reservoir characterization is required to successfully produce methane from hydrate bearing reservoirs. Therefore, imaging techniques are deployed to natural gas hydrate reservoirs to monitor essential reservoir parameters such as electrical or seismic properties on a field scale.

Bauer *et al.* (2005) performed a cross-well tomography at the Mallik 5L-38 gas hydrate production research well to monitor the elastic parameters such as seismic velocities, attenuation and anisotropy of the hydrate bearing sediment layers. Using marine controlled source electromagnetics, Schwalenberg *et al.* (2010) investigated the electromagnetic properties on active ocean-continent collision regions on the Hikurangi Margin, offshore New Zealand,

to verify seismical and geochemical evidences for the presence of gas hydrates.

Reducing the complexity of field experiments, the mechanisms accompanying hydrate formation and dissociation still raise questions even on a pilot scale. The nucleation of hydrates strongly depends on the type of hydrate formation (at a gas–water interface or from the dissolved phase) and the sediment (Rydzy 2013). In addition, gas migration during hydrate decomposition depends on the specific spatial distribution of hydrates in the pore space and can significantly differ each time. To better understand how and where hydrates form and to detect the pathways of the produced free gas phase, imaging techniques are essential at all scales, field tests as well as laboratory experiments.

Ersland *et al.* (2009) monitored hydrate formation and subsequent CO_2 injection in a high pressure cell using a magnetic resonance imaging (MRI) technique. Analysing these MRI data they were able to determine the amount and the distribution of water, free gas and methane hydrates in Bentheim sandstone core plugs. Kneafsey *et al.* (2007) monitored local density changes in a pressure vessel during hydrate formation and dissociation using X-ray computed tomography (CT). They observed potential mineral grain shifting as a response to hydrate formation and dissociation and significant water migration. However, X-ray CT relies on density. Since the densities of (sea)water and hydrate are very similar, X-ray CT measurements are not sensitive to hydrate formation from a dissolved phase without a free gas phase. This problem can be avoided by adding relatively heavy salt ions to the pore water increasing the pore water's density (Rydzy 2013), though one has to keep in mind that dissolved salt ions reduce the CH_4 solubility, thus altering the hydrate equilibrium conditions. As it is assumed that hydrate formation from methane dissolved in water more closely explains the formation of natural, marine gas hydrates in sandy formations (Buffett & Zatsepina 2000), efforts are required to develop experiments allowing for geophysical monitoring of the formation of hydrates from dissolved CH_4 and their dissociation.

Therefore, a LArge Reservoir Simulator (LARS) has been developed in the framework of the German national gas hydrate project SUGAR (Schicks *et al.* 2011, 2013). This reservoir simulator permits the formation of gas hydrates from methane-loaded brine under simulated *in situ* conditions mimicking marine scenarios. LARS is equipped with a series of sensors: different types of instrumentation can be used allowing for live temperature monitoring within the sediment sample. A cylindrical electrical resistivity tomography (ERT) array composed of 375 electrodes is used to monitor the formation and dissociation of gas hydrates within LARS. A good ERT-resolution is granted by the large electrical contrasts in the pore space, as the present phases of non-conducting sediment, well conducting saline pore fluid, and poorly conducting hydrates cover a wide range of electrical properties. During the respective hydrate dissociation, the stationary high-resistive hydrate phase converts into an isolating but mobile free gas phase. Thus, significant changes of the sediment's electrical properties are expected throughout the entire hydrate evolution, suggesting the use of an ERT array.

This study presents data of three hydrate formation experiments. In particular we focus on the ERT and temperature data of two hydrate formation experiments filling ≈90 per cent of the sediment's pore space (LARS RUNs 2 and 4) and the subsequent hydrate dissociation experiments. The latter simulated the 2008 Mallik production test, where the pressure was reduced in several steps. Furthermore, we show how local hydrate saturation and permeability changes during hydrate formation can be estimated using a data processing routine based on commonly applied models.

Table 1. Summary of relevant parameters used for the ERT measurements.

Electrode configuration:	Circular dipole–dipole
Stacking	10 x
Input current	1 mA
Frequency	25 Hz
Measurement interval	4 h
Measurement duration	25–30 min

2 LARS, ERT AND EXPERIMENTAL PARAMETERS

To investigate the formation and dissociation of gas hydrates under simulated *in situ* conditions, a LARS has been developed. Within the LARS, hydrate is formed from methane-loaded saline water circulating through a 210 litre sediment sample. Thus, no free gas phase is present in the sediment sample until hydrate dissociation is initiated. So far, hydrate dissociation in LARS has been initiated by depressurization or thermal stimulation, using an implemented counter-current heat-exchange reactor. For a detailed description of both, LARS and the heat reactor, see Schicks *et al.* (2011, 2013).

A cylindrical ERT array has been installed in LARS to acquire new knowledge on the spatial distribution of hydrate growth in the sediment sample. The ERT features 375 electrodes arranged in 25 circular rings with 15 electrodes in each ring. The tomographical array installed in LARS and its data quality are described elsewhere (Priegnitz *et al.* 2013). As ERT measurements always provide an inverse problem, the measured data has been processed using the inversion software Boundless Electrical Resistivity Tomography BERT (Günther *et al.* 2006). Table 1 lists the relevant parameters used for the ERT measurements.

We performed three hydrate formation experiments in LARS filling as much as 89.5 per cent (LARS RUN 2), 50 per cent (LARS RUN 3) and 90 per cent (LARS RUN 4) of the sample's pore space, respectively. The sediment sample used for the experiments LARS RUNs 2 and 3 was a medium to coarse quartz sand with a narrow grain size distribution of ≈89 per cent within the interval of 500–1000 μm. The corresponding initial porosity was 35 per cent. The respective permeability at ambient conditions was determined to be 673 ± 11 *D*. LARS RUN 4 featured a slightly coarser quartz sediment sample with 98.5 per cent of the sand being in the interval 500–1000 μm. The corresponding porosity and permeability were determined to be 39.2 per cent and 2030 *D* ± 23 *D*. The pore fluid in all three experiments was a 3.68 g l^{-1} NaCl-water solution with an initial conductivity of ≈6.5 mS cm^{-1}. The saline pore fluid was loaded with CH_4 in a gas-water interface chamber and injected into the sediment sample. To avoid clogging by hydrates at the fluid inlet, the methane-loaded saline water entered the sample at a temperature 3–4 °C above the hydrate stability temperature for a given pressure. This small temperature shift still allowed methane concentrations close to saturation in the pore fluid (Spangenberg *et al.* 2015). Inside the sediment sample hydrate stability conditions were achieved by active cooling of the sample's surrounding (T_{conf} = 4 °C). The rapid temperature drop decreased the methane solubility of the pore fluid. The resulting supersaturation (excess methane) was available for hydrate formation. Waite & Spangenberg (2013) showed that the degree of excess methane is in the order of 40 per cent of the initial methane concentration. After migrating through the sediment sample, the pore fluid was reloaded with CH_4 and entered the sample again. The pore pressure was held constant at 11 MPa throughout the hydrate formation experiments. By circulating the methane-loaded

pore fluid through the sediment sample we were able to achieve hydrate saturation rates of up to ≈2 per cent per day.

The LARS RUN 4 experiment was destined to examine the hydrate formation and dissociation patterns observed in LARS RUN 2 with a different sediment material as well as a different temperature sensing technique and to ideally proof the reproducibility of our experiments. During LARS RUNs 2 and 3, the temperature within the sediment sample was measured using 14 spatially distributed PT100 temperature sensors. PT100 sensors generally yield very accurate temperature data, though they cover very little area. Prior to LARS RUN 4 the spatially distributed PT100 sensors were replaced by a distributed-temperature-sensing (DTS) coil. A total length of ≈11 m DTS coil meandered throughout the specimen allowing increased spatial coverage. However, the installed DTS system yielded averaged temperature values for 0.5 m intervals, reducing the spatial sensitivity.

The injection of relatively warm methane-loaded pore fluid produced an inhomogeneous temperature field in the sediment sample. Because the electrical resistivity varies with temperature, the most accurate results were obtained by stopping the circulation to produce a homogeneous temperature field for the ERT measurements. Hence, methane saturated pore fluid was continuously circulated for five days, increasing the specimen's hydrate saturation by approximately 10 per cent (referred to as injection period). After this period circulation was stopped to ensure thermal equilibrium within the sediment sample. ERT measurements were performed every four hours throughout the entire hydrate formation experiments, providing data for both thermal equilibrium and non-equilibrium states.

3 ESTIMATING LOCAL HYDRATE SATURATION AND PERMEABILITIES

The inverted resistivity data obtained from ERT measurements serve as an indirect measure of the hydrate content in the pore space. Since the solid hydrate phase is directly related to the electrical and hydraulic properties of the pore space, the resistivity distribution can be converted into the distribution of hydrate saturation S_H and permeability K.

3.1 Hydrate saturation

The bulk hydrate saturation during the hydrate formation experiments has been determined by frequent pore fluid sampling. During hydrate formation only fresh water is consumed, while dissolved salt ions accumulate in the residual pore fluid, increasing the electrical conductivity. Following Spangenberg & Kulenkampff (2006), the variations of pore fluid conductivity can be converted into the mass of produced methane hydrate and hydrate pore space saturation as follows: The NaCl concentration of the pore fluid is linked to the electrical conductivity by

$$c = \frac{\sigma}{\Lambda_{\mathrm{eq}}} \tag{1}$$

where c is the NaCl concentration, σ is the measured electrical conductivity of the pore fluid and Λ_{eq} is the equivalent conductivity. Considering the mass fraction of a solution with an initial NaCl concentration c_0, the mass of water consumed in hydrate formation at a certain time t can be calculated using

$$m_{w-h}(t) = m_{w_0}\left(1 - \frac{c_0}{c(t)}\right) \tag{2}$$

where m_{w-h} is the mass of water consumed in hydrate formation at a given time t, m_{w_0} is the mass of water present at the very beginning of the experiment, and c_0 and $c(t)$ are the NaCl concentrations at the beginning of the experiment and at time t, respectively. Based on the methane hydrate composition $CH_4 \bullet 5.9H_2O$ (Stern *et al.* 2003) and the density of methane hydrate ρ_{hydrate}, the mass of produced hydrate m_{hydrate} can be determined from the water consumption m_{w-h}. Additionally considering the sample's pore volume V_{pore} allows to calculate the bulk hydrate saturation

$$S_{\mathrm{hydrate}} = \frac{m_{\mathrm{hydrate}}}{V_{\mathrm{pore}} * \rho_{\mathrm{hydrate}}} \tag{3}$$

For all LARS RUNs, these bulk hydrate saturation values served as a reference baseline to verify the saturations gained from the ERT data.

Converting the electrical resistivity distribution obtained from the ERT data into the distribution of hydrate saturation requires an eligible relation considering the electrical properties of the present phases. During hydrate formation, the pore space is filled with two coexisting phases: the pore fluid of high electrical conductivity and hydrates, which can be considered to be an electrical insulator. Commonly, Archie's equations (Archie 1942) are used to determine the effective electrical properties in a multiphase system where the majority of the electrical charge transport is sustained by the pore fluid. Though we tested several mixing rules (Garnett-Maxwell 1904; Lichtenecker 1926; Landauer 1952; Waff 1974), we decided to use Archie's equations for two reasons: (1) the obtained results in our experimental setup should remain comparable to other published data sets which typically used Archie's equations; and (2) we found that applying Archie's equations yielded the most comprehensible results.

Thereby, we investigate Archie's equation in two different terms:

(i) Archie$_{var-phi}$ interprets the increasing hydrate phase as part of the (also non-conductive) sediment grain framework resulting in a decreasing porosity while hydrate saturation increases. The pore space, however, is completely fluid-saturated at all stages of hydrate saturation and the first Archie equation is used:

$$\rho = \frac{a}{(\Delta\phi)^m}\rho_{\mathrm{fl}} \tag{4}$$

where ρ is the bulk resistivity for a sample fully saturated with a fluid of resistivity ρ_{fl}. a and m are empirical parameters and were set to 1 and 1.5, respectively, according to the effective medium theory (Sen *et al.* 1981). $\Delta\phi$ is the varying porosity $\phi - \phi S_H$, depending on the degree of hydrate saturation S_H.

(ii) Archie$_{var-sat}$ interprets the increasing hydrate phase as a decrease of fluid saturation in the pore space. Thus, the porosity remains constant whereas the water saturation varies with different amounts of pore filling hydrate and the second Archie equation is used:

$$\rho = \frac{a}{\phi^m S^n}\rho_{\mathrm{fl}} \tag{5}$$

with

$$S = \frac{\phi - \phi S_H}{\phi} = 1 - S_H \tag{6}$$

where S is the pore water saturation depending on the degree of hydrate saturation and n is an empirical parameter (saturation exponent) set to 1.9386 (Pearson *et al.* 1983).

As the two Archie equations account for different parameters, the corresponding resistivities governing the degree of hydrate saturation differ as well. Fig. 1 shows the modelled resistivity evolution for

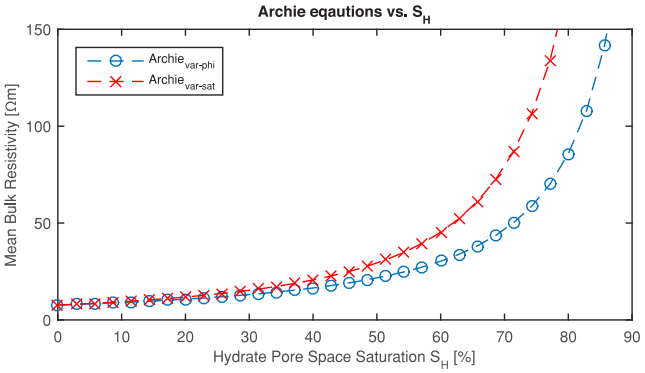

Figure 1. Modelled resistivity evolution of the two Archie interpretations Archie$_{var-phi}$ and Archie$_{var-sat}$ during hydrate saturation.

both Archie approaches within the experimentally covered hydrate saturation interval of 0–90 per cent.

To apply both Archie equations to the ERT data, we established the following data processing routine: In a first step, the inversion created a mesh dividing the sample volume into a total of 41 840 volume cells. Subsequently the inversion algorithm yielded resistivity data for a temperature of $T_M = 4\,^{\circ}$C for every single volume cell. Since the electrical resistivity varies with temperature the resistivity value of each cell was corrected against temperature to its reference value at $T_{\mathrm{Ref}} = 20\,^{\circ}$C. Rearranging both Archie approaches (eqs 4 and 5) for S_H, we were able to apply those relations to every single volume cell to estimate the local hydrate saturation.

The two Archie approaches were applied to the measured ERT data. Because the most significant differences among those mixing laws were expected at bulk hydrate saturation degrees of >50 per cent (see Fig. 1), we compared the results applying the different relations to the LARS RUN 2 data set of $S_H \approx 90$ per cent, which equals the highest saturation value in this experiment. (Fig. 2).

Both Archie approaches yielded comprehensible results. However, Archie$_{var-phi}$ generated a maximum local hydrate saturation value of 94.2 per cent, whereas Archie$_{var-sat}$ produced 88.9 per cent. At all stages of bulk hydrate saturation, Archie$_{var-phi}$ resulted in higher saturation values compared to those obtained with Archie$_{var-sat}$, with a difference always smaller than 10 per cent. As the maximum local hydrate saturation value generated by Archie$_{var-sat}$ was smaller than the reference bulk hydrate saturation obtained from pore fluid sampling, we considered Archie$_{var-phi}$ to yield the best results.

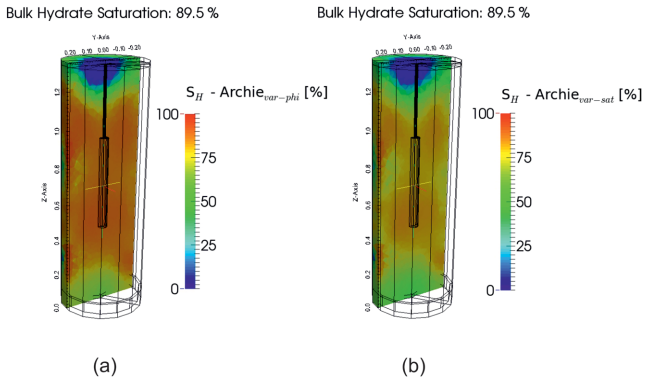

Figure 2. Application of the two Archie approaches to the final saturation stage of $S_H \approx 90$ per cent. Hydrate distribution obtained by applying (a) Archie$_{var-phi}$ and (b) Archie$_{var-sat}$.

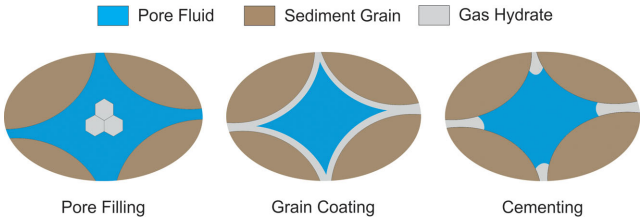

Figure 3. Illustration of pore filling, grain coating and cementing hydrate.

3.2 Permeability

The permeability as a material's hydraulic property is hard to capture using non-hydraulic measurement techniques. Generally, fluid flow is controlled by the interconnected pore space. In hydrate bearing sediments hydrate can affect both, the geometry of pores (pore-filling) and the interconnectivity of the sediments pore space, as hydrates formed at grain contacts might clog pore throats (grain coating, cementing) (Fig. 3).

Nevertheless, numerous approaches have been established to link the permeability to flow-affecting petrophysical parameters such as pore space geometry. The University of Tokyo introduced a very simple but effective relation to evaluate the permeability of a hydrate bearing sediment layer (Minagawa *et al.* 2005):

$$K(S_H) = K_0(1 - S_H)^N \tag{7}$$

with S_H being the fractional degree of hydrate saturation, K_0 the initial permeability at $S_H = 0$ and N being constant. Apart from S_H the only parameter affecting the permeability is the exponent N. Reported values for N range from 2.5 to 15 (Minagawa *et al.* 2005; Delli & Grozic 2013). It has been shown that values of N have to be chosen carefully to match experimental data and strongly depend on the investigated sediment. Since we do not have any experimental permeability data of the LARS sediment for the different stages of hydrate saturation, we are not able to identify a reasonable value for N, necessitating an alternative relation.

Another common approach relating the hydraulic permeability to petropysical parameters is the Carman-Kozeny (CK) relation (Carman 1956). CK originally relates the permeability to a geometric factor B, the porosity ϕ, the tortuosity τ and the specific surface area S (Mavko *et al.* 2003):

$$K = \frac{B\phi^3}{\tau^2 S^2}. \tag{8}$$

The CK relation can also directly be related to the degree of hydrate saturation (Kleinberg *et al.* 2003):

$$K(S_H) = K_0 \frac{(1 - S_H)^{n+2}}{(1 + \sqrt{S_H})^2} \tag{9}$$

where n is the saturation exponent with $n = 0.7S_H + 0.3$ (Spangenberg 2001; Delli & Grozic 2013). It should be noted that eq. (9) is only valid for pore filling hydrate formation, but not for hydrates coating the sediment grains or clogging pore throats (Fig. 3) (Kleinberg *et al.* 2003). Because the sediment's pore space in our experiments is completely water saturated at all times throughout hydrate formation and hydrates are formed from methane dissolved in the pore water, we assume to mimic the formation of natural, marine gas hydrates. Recent studies (Konno *et al.* 2015; Santamarina *et al.* 2015) carried out on natural sediment cores obtained from a methane hydrate reservoir in the Eastern Nankai Trough indicated from permeability and velocity measurements that natural, marine hydrates form and accumulate in the centre of the pores, justifying the assumption made by eq. (9).

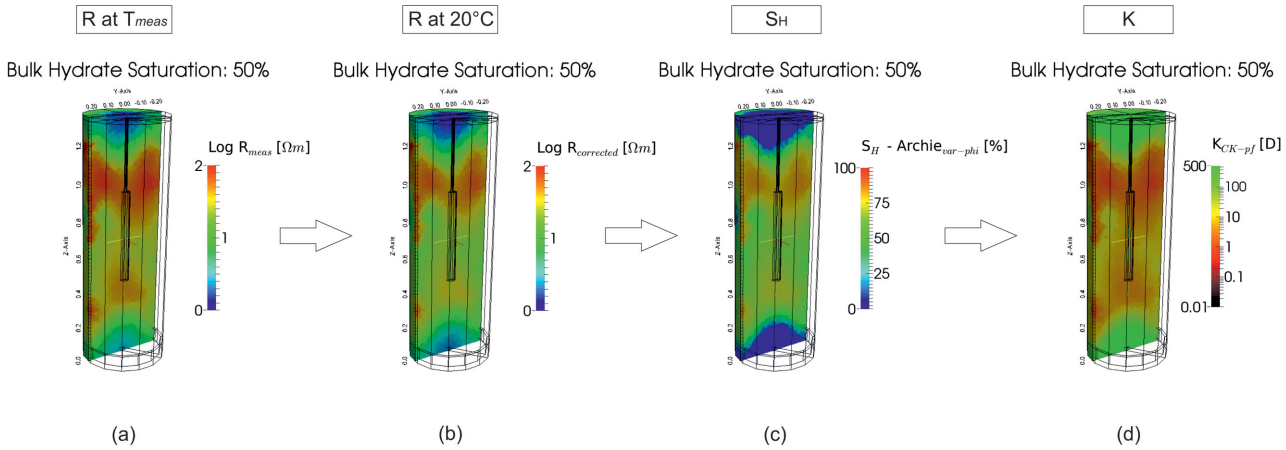

Figure 4. Illustration of the applied workflow to obtain the distribution of hydrate saturation and local permeability for a single measurement. (a) The inversion yielded the resistivity distribution at a temperature of 4 °C. (b) For comparability, the initial resistivity values got corrected against temperature to their reference value at 20 °C. (c) Those reference values were used to estimate local hydrate saturations S_H using Archie. (d) The determined S_H values were used as input data to estimate local permeability values.

Since the highly permeable sediment volume is very large, we unfortunately were not able to experimentally determine the initial permeability K_0 because the pressure gradients within the sediment were in the error range for the installed pressure sensors at low and intermediate bulk hydrate saturations. In a first order approximation, we therefore derived the initial permeability K_0 by applying empirical approaches considering the sample's grain size distribution (Hazen 1893; Terzaghi 1955). As the resulting permeability values covered several orders of magnitude, we chose to determine the sediment's K_0 at ambient pressure and temperature by conducting a Darcy fluid flow experiment. The resulting permeability was $K_0 = 673 \pm 11$ *D*. Since the experiments in LARS were run at a differential pressure of 4 MPa, the sediment's pore space experienced compaction and grains possibly cracked. Taking this into account, we set the initial permeability to $K_0 = 500$ *D*.

Regarding the data structure, the permeability value of each volume cell was determined using the (previously obtained) S_H value of the respective volume cell (see Section 3.1) in eq. (9). The described workflow is illustrated in Fig. 4.

4 RESULTS

4.1 Hydrate formation

During LARS RUN 2, a maximum bulk hydrate saturation of ≈90 per cent was reached at a constant pore pressure of 11 MPa. The fourteen temperature sensors (11 operating, 3 broken) were spatially distributed in the sediment sample to allow for the identification of the spatial extend of the hydrate stability zone within the specimen. The positioning of the PT100 sensors is shown in Fig. 5. We started the experiment by circulating the methane-loaded saline pore fluid from top to bottom.

Fig. 5 shows the temperature profiles of the sensors T1–T4 for the first four weeks of the hydrate formation experiment with the dashed line marking the hydrate stability temperature of 13.3 °C at given pressure. The Roman numbers mark the pore fluid injection periods. As long as no fluid was injected, the reservoir's base-temperature was defined by the confining temperature ($T_{\text{conf}} = 4$ °C). The methane-loaded brine entered from the top of the sample at a temperature slightly above hydrate stability conditions (≈16 °C)

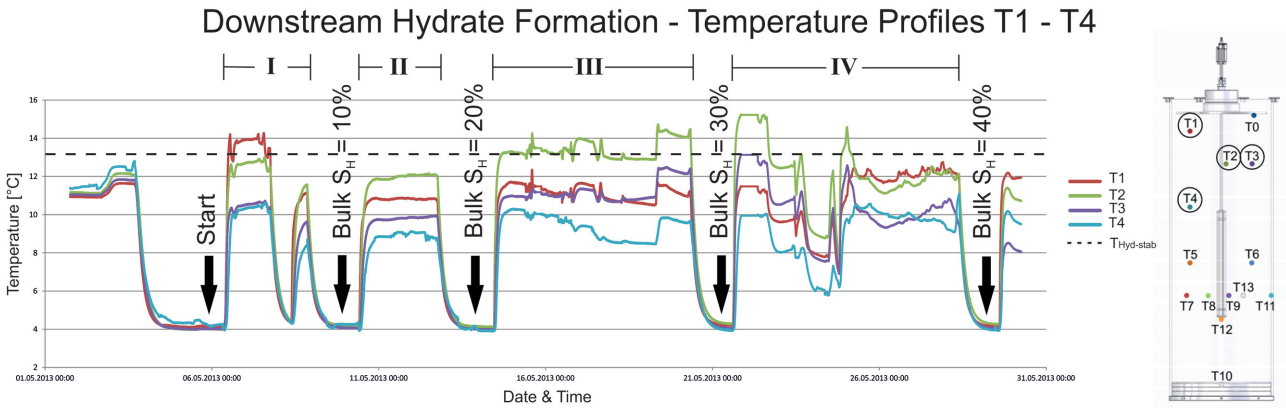

Figure 5. Temperature profiles of the sensors T1–T4 during hydrate formation from downward fluid flow with a sketch of LARS and the positions of the temperature sensors on the right. Roman numbers mark the intervals of pore fluid injection. The methane-loaded brine entered the sample at a temperature of ≈16 °C and was cooled down due to active cooling from the surrounding (4 °C). The hydrate stability temperature of 13.3 °C at 11 MPa is marked with the dashed line. The rapid temperature drops to 4 °C between two injection intervals were due to the stoppage of fluid circulation to let the sample thermally equilibrate for ERT data processing.

and cooled down until hydrate stability temperature was reached while circulated through the sediment due to the active cooling from the surrounding. During the first pore fluid injection period, the highest temperatures (≈14 °C) were recorded at sensor T1, as the injected pore fluid reached this sensor first. After each injection period, the fluid circulation was stopped to let the sediment sample equilibrate thermally. During the second injection period, the highest temperatures were recorded at sensor T2, indicating that the comparably warm pore fluid did not reach sensor T1 as much as before. The decrease in heat supply was caused by hydraulic constraints due to the formation of a solid hydrate phase at the very top of the reservoir around sensor T1. During the third and fourth injection period, sensor T1 displayed temperatures even lower than T3, suggesting continuous hydrate formation at T1 while T3 was located in the fluid path. The temperature sensor T4 almost continuously recorded the lowest temperatures, as the injected pore fluid was cooled down until it reached T4. Thus, the cooling from the surrounding exceeded the heat supply from the pore fluid. As the temperatures at T4 were always within the hydrate stability field, the majority of the supplied methane is assumed to be bound in hydrate before it could reach T4. Temperatures recorded at a sensor located in the centre of the sample (T2) where higher at all times and suggested that hydrates predominantly formed in the boundary regions of the sample, where cooling was strongest. Following the first injection period the temperatures recorded at T2 were continuously higher than those recorded in the boundary regions (T1, T3, T4), indicating an elevated heat supply from the injected pore fluid. Whereas the elevated driving forces (lowest temperature) close to the wall urged hydrate to form and to hydraulically constrain the fluid pathways, the centre of the sample still experienced sufficient heat supply to maintain pathways for the injected fluid.

Hydrate formation in the top boundary regions during downward fluid circulation could be confirmed by ERT measurements. Fig. 6 presents the evolution of spatial hydrate distribution and local permeability changes for the entire hydrate formation experiment applying the Archie$_{var-phi}$ and CK relation, respectively. It should be noted that the top and bottom 15 cm in the ERT-figures are not covered by electrodes and thus constitute an extrapolation of the inversion algorithm. At the very beginning of the experiment uniform hydrate saturations of 0–5 per cent were observed. During the following saturation stages, the majority of the hydrate phase formed in the upper 60–70 cm of the sediment sample. At a bulk hydrate saturation of 40 per cent calculated from the pore water conductivity measurements, hydrate began to form in lower regions of the sample while areas in the top of the reservoir showed hydrate saturations in the order of ≈80 per cent. To avoid hydraulic clogging at the top of the sample, the fluid circulation direction was switched from downwards to upwards. This led to an immediate increase of local hydrate saturation in the lower regions of the sample. Subsequently, hydrate formation advanced until almost the entire sample showed high saturation values. At the final saturation stage of 89.5 per cent the fluid pathways in the sediment were almost clogged and the fluid circulation was switched off.

Eq. (9) shows that the permeability is directly linked to the local hydrate pore space saturation. Accordingly, the changes of local permeability strongly correlate with the changes in local hydrate saturation. At the beginning of the hydrate formation experiment an almost homogeneously distributed permeability of 500 D was observed, which is just the predefined K_0. The subsequent hydrate formation in the upper part of the reservoir reduced the permeability in the respective areas. When we switched the pore fluid's flow direction at a bulk hydrate saturation of 40 per cent, permeabilities were in the order of 10^1 D in the upper part of the reservoir. The reversed fluid flow increased hydrate pore space saturation in the lower parts of the reservoir, further reducing the permeability of the affected area. At the final stage of $S_H = 89.5$ per cent the minimum permeability value generated by applying CK was $K_{\min} \approx 28.8$ mD.

During the LARS RUN 4 formation experiment we generally observed similar formation patterns. By slightly increasing the pore fluid injection velocity at the beginning of the experiment, the hydrate stability isotherm (again 13.3 °C at 11 MPa) was shifted towards the centre of the specimen, so that initial hydrate formation was observed much more centric as in LARS RUN 2. Because both experiments yielded very high bulk hydrate saturation values at the final stage, the final hydrate distribution for both experiments appeared very similar (Fig. 7).

4.2 Hydrate dissociation

During hydrate dissociation it is not possible to clearly identify all present phases by only measuring the electrical properties, since both, the emerging free gas phase and the remaining gas hydrates, are electrically isolating. The ERT only discriminates between areas of conductive and non-conductive pore space. Please note, that the ERT images recorded during hydrate dissociation therefore do not show the colour-coded hydrate saturation, but the electrical resistivity in a log scale. For a detailed interpretation, it is therefore necessary to include additional data such as temperature, pressure, and fluid flow.

The hydrates formed in LARS RUN 2 (see Fig. 6) were dissociated by pressure reduction in two stages: (1) simulating the 2008 production test in Mallik, Mackenzie Delta, Canada via depressurization in three steps (e.g. Wright *et al.* 2011) at 7.0 MPa–5.0 MPa–4.2 MPa (see Fig. 8) followed by (2) depressurization to atmospheric pressure (see Fig. 9). To simulate the Mallik production test, the surrounding temperature was set to 11 °C and reservoir pressure was initially set to 11.5 MPa (Uddin *et al.* 2011). Noteworthy, what had been an active cooling (4 °C) from the surrounding during hydrate formation turned into an active heating during hydrate dissociation.

The experiment started with P–T conditions deep within the hydrate stability field (at 11 °C $P_{\text{stab}} = 8$ MPa). The first pressure reduction to 7 MPa induced an immediate temperature decrease of ≈1.6 °C due to endothermic gas hydrate dissociation (Fig. 8). The resulting temperature of 9.4 °C already fell below the surrounding temperature and corresponded to the hydrate stability temperature at given pressure (7 MPa). After the second depressurization to 5 MPa (≈3 hr), the temperature profile of T0 clearly displayed temperatures outside the hydrate stability field ($T_{\text{stab}} = 6.1$ °C at P = 5 MPa) indicating complete hydrate dissociation at the top of the reservoir. Unfortunately, the ERT inversion results did not yield reliable information about this specific area as the top 15 cm of the sample are not covered by electrodes. All other temperature profiles dropped to the hydrate stability temperature at given pressure, suggesting that the front of hydrate decomposition was initiated at the top end face of the sediment sample. During the third pressure reduction (4.2 MPa) the temperature close to the neoprene jacket (T11) increased (Fig. 8). This temperature increase indicated that the endothermic process of hydrate dissociation could not compensate the heat supply from the surrounding (11 °C) anymore. Due to the decreased hydrate content hydrate decomposition declined. The ERT inversion results of the regions close to the neoprene jacket after 6 h showed areas of considerably lower resistivity. As both,

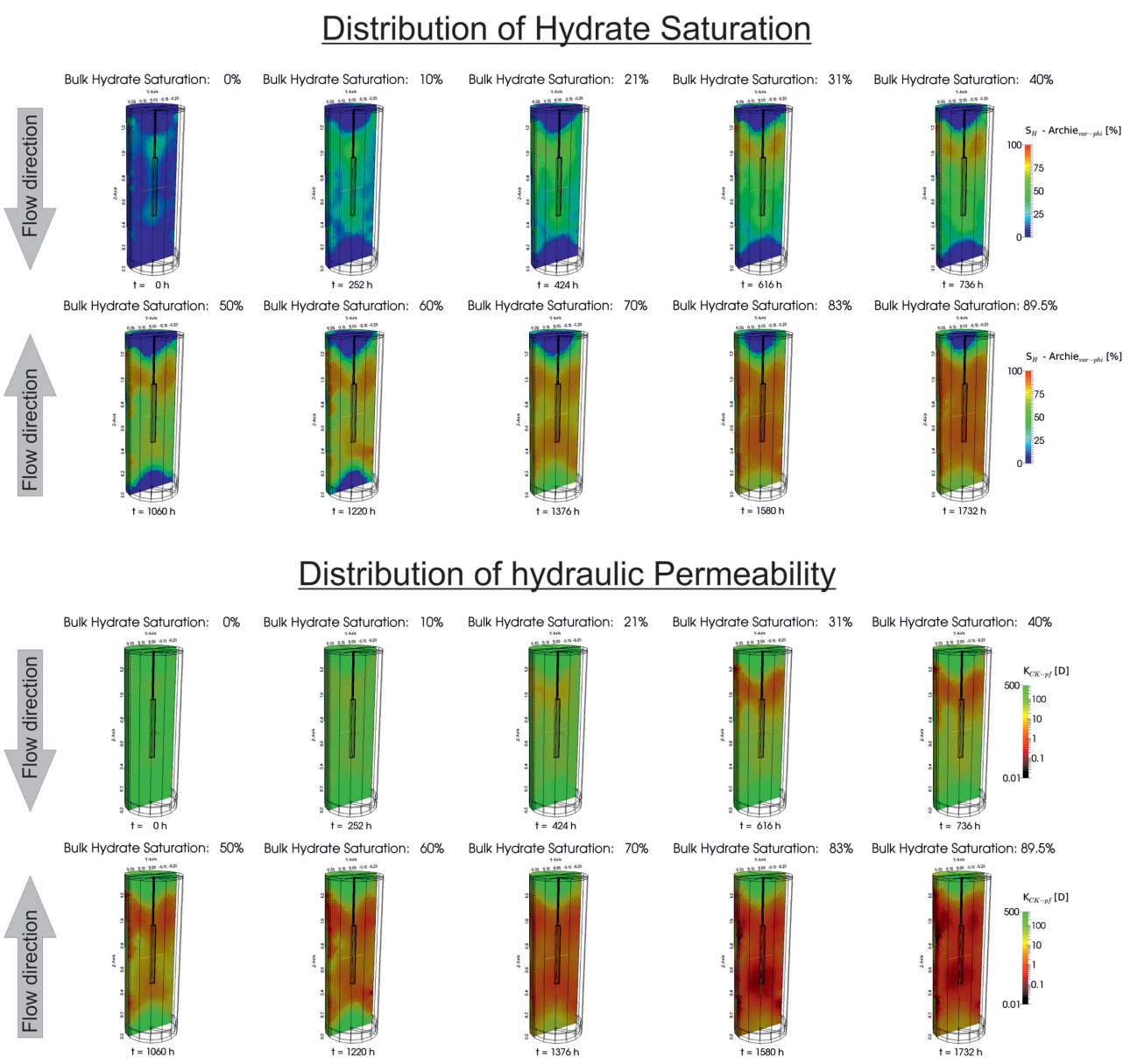

Figure 6. Results estimating the local hydrate saturation and permeability in the sediment sample applying Archie$_{var-phi}$ and CK to the ERT data. At a bulk hydrate saturation of 40 per cent, the pore fluid flow direction was switched to avoid clogging of the fluid flow paths as local hydrate saturations in the upper part of the reservoir reached 80 per cent. Generally, permeability decreases as hydrate saturation increases. At the stage of maximum bulk hydrate saturation, a minimum permeability value of $K_{\min} \approx 28.8$ mD was found.

hydrate and free gas, increase the electrical resistivity, the low resistivity values suggested completed hydrate dissociation and methane gas depletion in these regions (Fig. 8).

After 8 hr, the outlet was closed overnight. The reservoir temperature slowly adjusted to the surrounding temperature and the reservoir pressure increased to reach the hydrate equilibrium pressure of ≈8 MPa at 11 °C. Though the system was closed for 16 hours, the time was not enough for the reservoir to reach the equilibrium temperature of 11 °C. Due to the heat supply from the surrounding, hydrates continued to dissociate. Whereas the released gas phase increased the reservoir pressure, the endothermic nature of hydrate dissociation cooled the sample from the interior. Because hydrate dissociation continued as long as the PT conditions within the reservoir fell below the stability conditions of ≈8 MPa at 11 °C, the continuing cooling from the sample's interior delayed the temperature increase of the reservoir. The depressurization to atmospheric pressure was conducted from 24 hr onwards (Fig. 9).

The rapid pressure drop to 0.1 MPa set the entire sediment sample out of the hydrate stability field. This was followed by a significant temperature drop due to rapid hydrate dissociation, leading to temperatures below the freezing point in the centre of the sample. Both, the ERT inversion results and the corresponding temperature profiles of T4, T9 and T12 showed the formation of ice in the centre of the sample (Fig. 9). Subsequently, the temperatures at all sensors continuously increased to adjust with the surrounding temperature of 11 °C. After ≈35 hr all temperatures were above the freezing point, suggesting that only water and free gas remained in the pore space. Thus, the remaining high resistivity areas in the ERT inversion results were caused by free gas trapped in of the sediment sample.

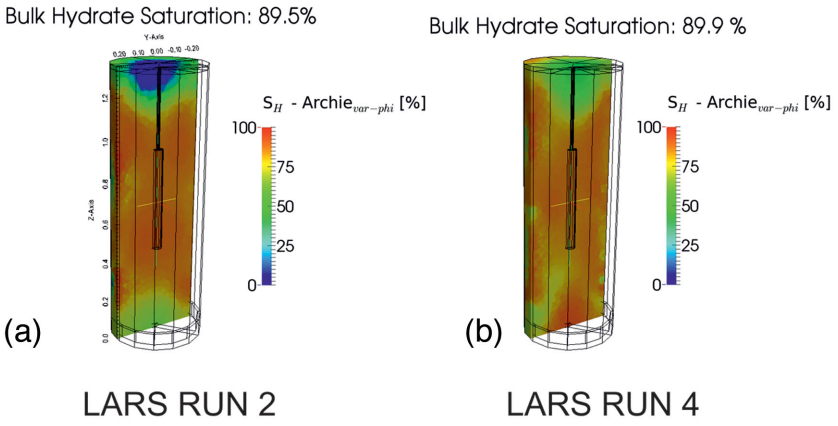

Figure 7. Final hydrate distributions at the end of the hydrate formation experiments of LARS RUNs 2 and 4.

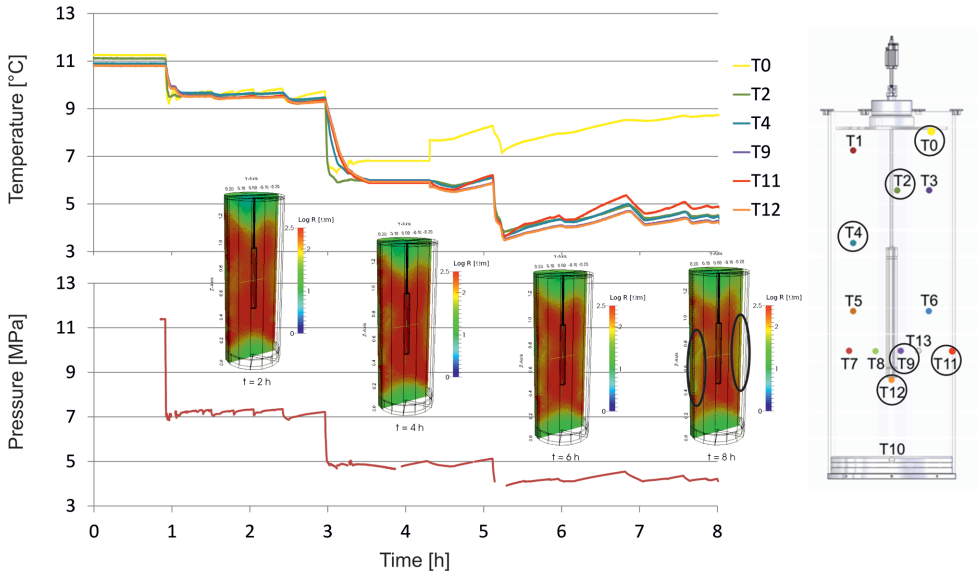

Figure 8. Overview of the first 8 hr of LARS RUN 2 depressurization. The conducted pressure levels are shown in the lower chart. The corresponding temperature profiles are shown in the upper chart and a sketch of LARS including the positions of the temperature sensors is given on the right. Depressurization was initialized by pressure reduction at the reservoir's top outlet. The temperature increase at T0 from the end of the first pressure step (≈2 hr) onwards indicates that hydrates at the very top were dissociated. From ≈4 hr onwards, the temperature at T11 starts to increase, indicating that the heat supply from the surrounding exceeded the energy loss caused by endothermic hydrate dissociation. The corresponding ERT inversion results also suggest hydrate dissociation in the boundary regions (black ellipses).

The hydrate phase formed during LARS RUN 4 was decomposed via depressurization as well, applying the same surrounding temperature (11 °C) and pressure levels as in LARS RUN 2 with an additional 3 MPa pressure level (Stage 1: 7.0 MPa–5.0 MPa–4.2 MPa–3 MPa; Stage 2: to P_{atm}). Because the experimental setup of LARS RUN 4 featured optical temperature measurements using a meandering DTS coil within the sediment sample, the number of temperature measurement points was significantly increased. However, as each data point provided by the DTS system constituted a mean temperature value for a 0.5 m interval it was necessary to evaluate the accuracy of the obtained DTS data. Therefore, three PT100 sensors were additionally placed on the cylindrical heat reactor in the centre of the sample. To investigate the comparability of both measurement techniques it was reasonable to evaluate the temperature data recorded during the decomposition experiments, as the various pressure drops induced much more significant temperature changes compared to those during the hydrate formation experiments. Fig. 10 presents the temperature data recorded at the PT100 sensor at the bottom of the heat exchange reactor (T0, blue) together with the DTS data obtained by the measurement interval corresponding to DTS point 19 (red) for the first 16 hr of the dissociation experiment. Because the measurement interval of DTS point 19 radial symmetrically surrounded the T0 sensor, the measured temperatures at those two points should be similar. With a recorded maximum deviation of 0.3 °C (in Fig. 10 at ≈3 hr) we considered the DTS data to give a good reflection of the temperature distribution within the sediment sample. Based on the obtained DTS data it was possible to extensively display the temperature evolution in the sediment sample during the LARS RUN 4 dissociation experiment.

At the first depressurization stage with the applied pressure levels of 7, 5, 4.2 and 3 MPa both the ERT and the temperature recordings yielded very similar dissociation patterns as observed in LARS RUN 2. Hydrate dissociation initiated at the top and in the boundary regions, where the pressure and temperature gradients were the highest. Subsequently, the dissociation front migrated towards the centre of the sample. Each pressure drop was accompanied by a

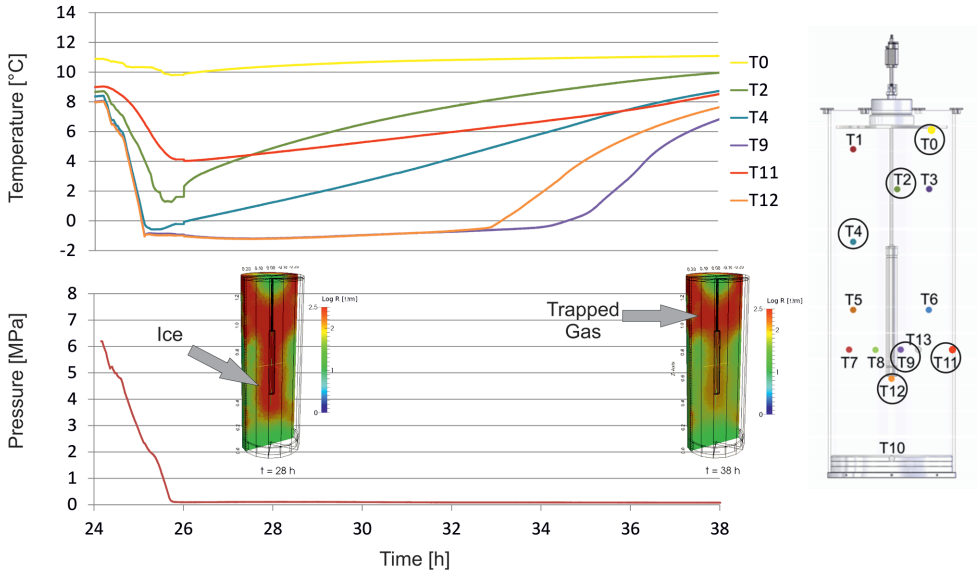

Figure 9. Continuation of LARS RUN 2 depressurization. During overnight valve closure, the reservoir pressure increased to the equilibrium pressure at 11 °C of 8 MPa. The depressurization was conducted to atmospheric pressure. Starting after ≈25 hr, the temperature profiles and ERT inversion results show that the centre of the sediment sample was frozen due to the rapid pressure drop accompanied by significant cooling. At this state, the boundary regions seem to be completely free hydrate and gas. At the final stage (38 hr), *P–T* conditions in the entire sediment sample were out of the hydrate stability field. The remaining high-resistivity areas in the ERT inversion results were caused by free gas which remained trapped in the upper parts of the sediment sample.

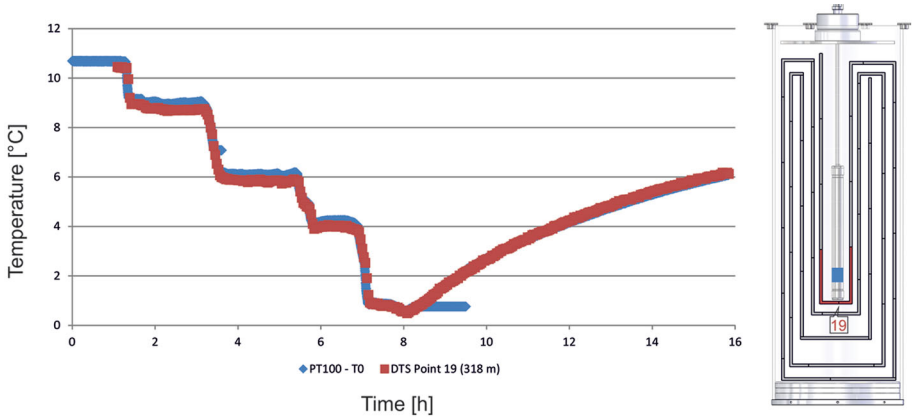

Figure 10. Comparison of the temperature data recorded by the PT100 sensor placed at the button on the heat exchange reactor (blue) in the centre of the sample and the DTS data obtained by the respective measurement interval of DTS point 19 (red).

temperature drop into the respective hydrate stability temperature. This can be seen, for example, on the temperature distribution of the 5 MPa pressure level in both LARS RUNs 2 (Fig. 8) and 4 (Fig. 11), having a hydrate stability temperature of ≈6.1 °C. Similar to the observations made in LARS RUN 2 the boundary regions of the sample appear to be almost completely free of any hydrate or free gas phase after 8 hr (Fig. 11). After the first 8 hours of the dissociation experiment the outlet was closed overnight again. During that time the temperature within the sediment sample started to adjust to the surrounding temperature of 11 °C, accompanied by a respective pressure increase. The LARS RUN 4 depressurization to atmospheric pressure was conducted from 27 hr onwards. Approximately three hours later, the endothermic nature of hydrate decomposition cooled the centre of the sample to temperatures below the freezing point again, resulting in ice formation in the respective areas (Fig. 12). After ≈36 hr all recorded temperatures were above the freezing point suggesting that all hydrates were dissociated and only water and free gas remained in the pore space.

5 DISCUSSION

5.1 Mixing laws

The choice of a proper mixing rule is a crucial point in our data processing routine. It turned out that the evaluation of proper mixing rule is a trial-and-error procedure. The suitability of a mixing rule not only depends on quantitatively matching the reference bulk saturation values, but also on qualitatively producing comprehensible hydrate distributions (e.g. in terms of saturation-heterogeneities). To test the different mixing rules it was necessary to apply them all to the measured ERT data and validate both their quantitative and qualitative appropriateness. In doing so the best results were obtained using Archie approaches. While Archie$_{var-phi}$ and Archie$_{var-sat}$ were very consistent, the highest local saturation values generated by Archie$_{var-sat}$ still fell below the bulk hydrate saturation obtained from pore fluid sampling.

During the hydrate formation experiments, the reference bulk hydrate saturation was determined by frequent pore fluid analysis (see

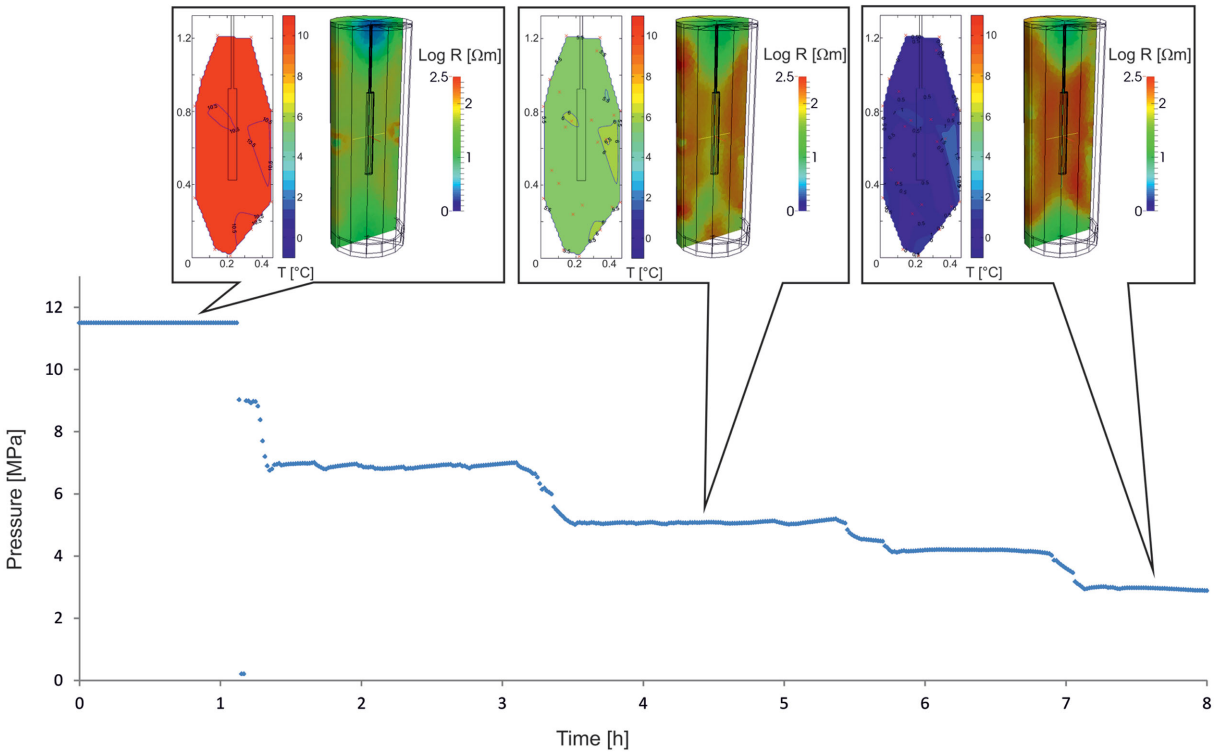

Figure 11. First 8 hr of LARS RUN 4 depressurization. The applied pressure drops to 7, 5, 4.2 and 3 MPa were accompanied by temperature drops to the respective stability temperature at given pressure (left in each balloon). Hydrate dissociation initiated at the top and the boundary regions of the sample. The latter appear to be methane-depleted after 8 hr.

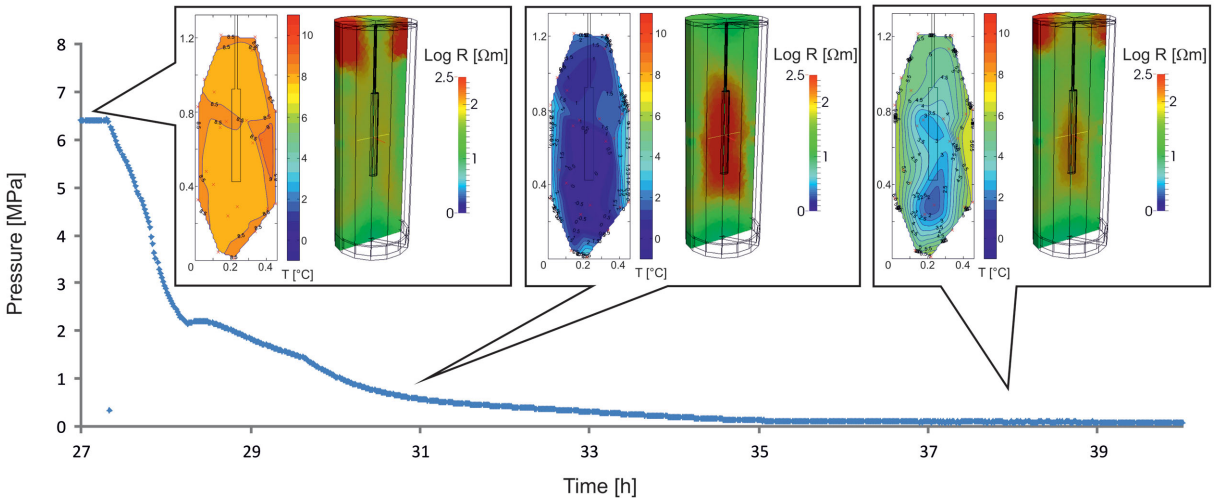

Figure 12. Continuation of LARS RUN 4 depressurization. During overnight valve closure, the reservoir temperature and pressure increased to adjust to the stability conditions at 11 °C. Due to the endothermic nature of hydrate decomposition, the depressurization to atmospheric pressure cooled parts of the sample to temperatures below freezing point again, resulting in ice formation.

paragraph 3.1). Since we applied Archie$_{var-phi}$ to the ERT data to determine local hydrate saturations, we could also determine values of bulk hydrate saturation from the ERT data. For this purpose the local hydrate content of all volume cells was summarized and related to the sediment's porosity. Comparing the bulk hydrate saturation values determined by pore fluid sampling and our ERT data processing routine was used to evaluate the quantitative eligibility of a mixing rule. Fig. 13 illustrates the evolution of the bulk hydrate saturation determined by applying Archie$_{var-phi}$ to the ERT data of LARS RUNs 2, 3 and 4 (solid lines) in relation to the reference values determined by pore fluid sampling (dashed line). It is evident that bulk saturations obtained by ERT data initially overestimated the reference bulk saturation by up to ≈10 per cent. Because the local saturation values were determined based on the measured resistivity distribution, the overestimated hydrate saturation had to be caused by increased resistivities obtained from the ERT. Closely looking on the initial hydrate distribution (0 per cent) in Fig. 6 shows that the majority of generated hydrate saturation is located right at the top and bottom of the implemented heat exchange reactor. Because the reactor was already fixed to the top cap of the pressure vessel

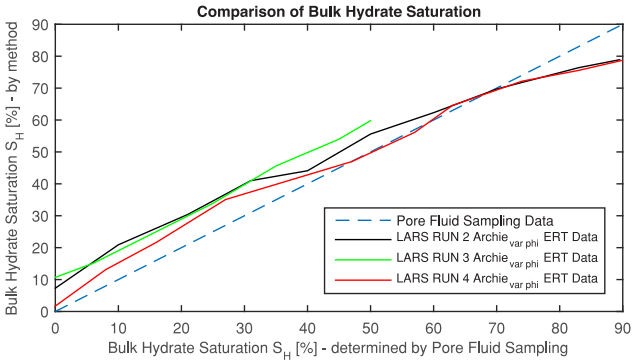

Figure 13. Comparison of bulk hydrate saturations determined by pore fluid sampling (blue dashed line) and bulk hydrate saturations obtained by applying Archie$_{var-phi}$ to the ERT data of LARS RUNs 2, 3 and 4 (solid black, green and red lines). The bulk hydrate saturation determined by pore fluid sampling is plotted on the *x*-axis and the bulk saturation determined for each method (pore fluid sampling and from ERT data) is plotted on the *y*-axis.

during the installation process, we therefore suggest that those areas experienced severe compaction during mounting. As a result, the porosity in the respective areas is suggested to be decreased, increasing the measured electrical resistivity and, thus, generated hydrate saturation in the ERT data.

For reference bulk saturation values exceeding 40 per cent, the bulk saturations obtained from ERT data of LARS RUNs 2 and 4 approximate the reference baseline. The LARS RUN 2 and 4 curves finally fell below the reference baseline at ≈70 per cent. Having such high degrees of bulk hydrate saturation, the possibility of hydrate forming hydraulic caps has to be considered. In such a case some water volume would be trapped and cut off from the circulation. The remaining water used for pore fluid sampling would subsequently overestimate the salinity within the sample, producing higher pore fluid sampling saturation values. In that case, the bulk saturation obtained from pore fluid sampling only yields an upper bound for a heterogeneous salinity distribution.

However, areas comprising a stable hydraulic sealing and trapping water should have been detectable in the ERT data, as the electrical properties in those areas would barely change over time. As visible in Fig. 6, such areas could not be identified. We assume that hydraulic caps might form during our hydrate formation experiments, but would last only for a relatively short time. The measured salinities during our formation experiments yielded an irregular increasing trend, giving evidences for the temporary existence of hydraulic sealings (Schicks *et al.* 2011). Spangenberg *et al.* (2015) emphasized that hydrates formed at high formation rates in LARS undergo recrystallization. If some areas were cut off from the circulation and, thus, from methane supply by solid hydrate caps, recrystallization is likely to re-establish the connection to the fluid circulation.

The underestimated saturation values obtained from the applied ERT data processing routine at high degrees of bulk hydrate saturation are therefore most likely caused by applying the Archie$_{var-phi}$ relation to the ERT resistivity data. Following eq. (4), a constant value for the exponent *m* (also referred to as cementation exponent) was used throughout all saturation stages. Because Archie$_{var-phi}$ interprets the increasing hydrate phase as part of the grain framework, a wide range of porosities are covered during our hydrate formation experiments. Since numerous studies considered *m* to be porosity dependent (e.g. Neustaedter 1968), efforts are required for future work to quantitatively determine appropriate Archie parameters throughout the entire range of bulk saturation achieved in our experiments. The same would be true for Archie$_{var-sat}$, because the saturation exponent might not be constant over the full saturation range, but depend on saturation (e.g. Spangenberg 2001; Spangenberg & Kulenkampff 2006).

However, since the saturation values determined by applying Archie$_{var-phi}$ qualitatively and quantitatively produced comprehensible results we consider them to follow the real distribution of local hydrate saturation, though the exact saturation values may differ by several percent.

5.2 Permeability

Based on the workflow presented in Fig. 4, local permeability changes could be estimated from the ERT data. The obtained resistivity distribution was converted into the spatial hydrate distribution, which served as input data for the CK relation (eq. 9). To evaluate the permeability estimates based on the ERT data, we averaged all local permeability values obtained during LARS RUNs 2 and 3 and compared them with modelled data derived from the CK equation (red dashed in Fig. 14). The LARS RUN 4 permeability data could not directly be related to the LARS RUNs 2 and 3 data sets since a different sediment sample with a much higher initial permeability K_0 was used. It is therefore not plotted in Fig. 14. The modelled permeability evolution of the CK relation yields a satisfactory fit for bulk hydrate saturations smaller 30 per cent. For bulk hydrate saturations exceeding 30 per cent, the permeability evolution obtained from the ERT data workflow increasingly overestimated the modelled permeability evolution. Unfortunately it was not possible to verify the estimated permeability distribution with measured values. Since the highly permeable sediment volume is very large, the pressure gradients within the sediment were in the error range for the installed pressure sensors at low and intermediate bulk hydrate saturations, so that it was not possible to directly measure the hydraulic bulk permeability during the experiments in LARS. Only one bulk permeability measurement could be carried out at the final stage of LARS RUN 2 ($S_H = 89.5$ per cent) with $k_{\min} = 5$ *mD* (green cross in Fig. 14). At this stage the obtained permeability overestimated the modelled CK relation by 2 orders of magnitude and the single measured data point by 3 orders of magnitude. Those deviations are most probably due to several reasons:

(i) The modified CK equation (eq. 9, red dash in Fig. 14) used in our workflow is a very simple equation which only considers

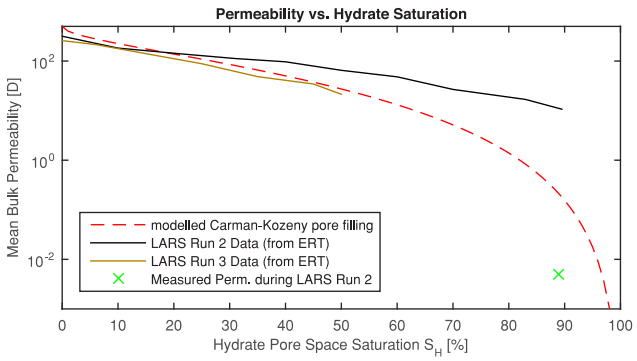

Figure 14. Comparison of modelled permeability (dashed line) and mean bulk permeabilities obtained during LARS RUNs 2 and 3 (solid brown and black lines) applying the introduced workflow.

the degree of hydrate saturation and neglects all sediment specific parameters. Subsequently, a homogeneous sediment sample as well as a homogeneous hydrate distribution are assumed, which is not the case in the LARS experiments (Fig. 6). Furthermore, deviations from ERT based S_H estimates consequently caused deviations in the permeability estimates, as S_H was the only input parameter in the CK relation.

(ii) Averaging anisotropic, heterogeneous data has to be carried out carefully. To pay tribute to direction-dependencies the single values can be interpreted as 'parallel connection' as well as 'series connection' requiring either the arithmetic or the harmonic mean. Furthermore the style of averaging significantly affects the resulting permeability evolution. For simplicity we averaged the obtained permeability data as a series connection by using arithmetic mean values. Using, for instance, harmonic mean values would cause the estimated permeability evolution to significantly underestimate the CK relation. Because the bulk hydrate saturation yielded by the ERT data workflow already underestimated the bulk saturation obtained from pore fluid sampling (see Fig. 13), this is most likely not the case.

(iii) The measured data point at $S_H = 89.5$ per cent constitutes the lower bound of the bulk permeability at this saturation stage. The experimentally obtained bulk permeability was determined by considering the differential pressure between the fluid inlet and outlet (at the sample's top and bottom). Thus, the experimentally measured permeability value was much more sensitive to plugging (due to sediment input and/or gas hydrate) in the capillaries, which generally reduces the measured permeability.

Though the estimated permeability values might show significant deviations, this information is valuable to qualitatively follow the permeability distribution during the formation experiments. Furthermore the obtained permeability distribution constitutes a helpful tool to adjust dissociation experiments.

5.3 ERT monitoring of hydrate formation and dissociation

Hydrate formation and dissociation were successfully monitored using ERT. The large contrasts in electrical properties between the coexisting pore filling phases granted hydrate localization even at low saturation.

During hydrate formation, ERT imaging and the recorded temperature profiles indicated that hydrate formed quickly within the sediment sample after reaching hydrate stability conditions. We modelled the temperature field within the sediment sample assuming an undisturbed fluid flow field (no hydrates present) using COMSOL Multiphysics (V. 4.3b) to identify the initial spatial extent of the hydrate stability field (Fig. 15). Fig. 15 shows the LARS RUN 2 resistivity distribution at a bulk hydrate saturation of 40 per cent (left) with the modelling results (right). The most significant resistivity increase occurred just after the injected pore fluid enters the hydrate stability field at a temperature of 13.3 °C. Evidently, the majority of the injected methane was consumed within hydrate formation as soon as it migrated into the hydrate stability field. The geometry and the spatial extent of the hydrate stability field thereby depend on the flow velocity and the temperature of the injected methane-loaded brine. However, by changing the flow velocity of the injected fluid and thus by shifting the hydrate stability temperature during the hydrate formation experiment of LARS RUN 4, the ERT and temperature recordings suggested that we have great

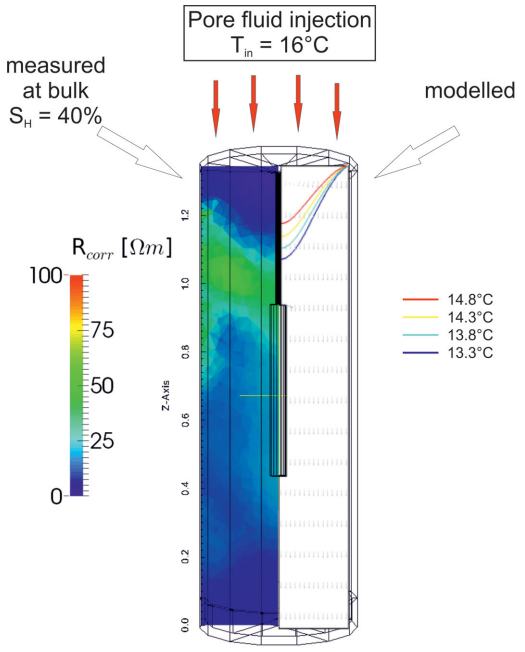

Figure 15. Comparison of measured resistivity distribution during LARS RUN 2 at a bulk hydrate saturation of 40 per cent (left) and the modelled temperature field resulting from active cooling from the surrounding (4 °C) and injection at the top end face of relatively warm pore fluid (≈16 °C). The isotherm of 13.3 °C marks the boundary of the hydrate stability field at 11 MPa.

control of the spatial extent of the hydrate stability field within the sediment sample.

Capturing the spatial distribution of remaining hydrates and free gas during hydrate dissociation is difficult. Both phases appear as electrically non-conductive, and therefore cannot be distinguished by only measuring the electrical properties of the pore filling. However, adding temperature and pressure data enables advanced interpretation of hydrate dissociation experiments in LARS.

Hydrate dissociation initialized at the top of the sediment sample, where the pressure gradient was highest. Subsequent hydrate dissociation was predominantly measured at the boundary regions of the sample, where the heat supply from the surrounding led to temperatures exceeding the hydrate stability temperature at given pressure. The ERT data identified the high-resistivity areas filled with hydrate and/or gas. We observed considerable resistivity increases in areas featuring active hydrate dissociation and, thus, gas release compared to areas exclusively filled with gas hydrate (Fig. 16). For pore filling hydrates, a water shell adsorbed at the sediment grain remains for $S_H < 1$ (Spangenberg 2001; Kuhs *et al.* 2014). The expanding free gas phase arising due to hydrate dissociation pushed this remaining pore water out of the pores, increasing the electrical resistivity. Thus, electrical measurements also enable to identify the onset of hydrate decomposition in the sediment's pore space.

6 SUMMARY AND CONCLUSION

The electrical properties of methane-hydrate bearing sediments were investigated during hydrate formation and dissociation experiments using an ERT array in the large reservoir simulator LARS. For the first time, it was possible to qualitatively visualize the occurring hydrate phase during hydrate formation experiments in LARS. The ERT measurements showed that hydrate formation started as soon

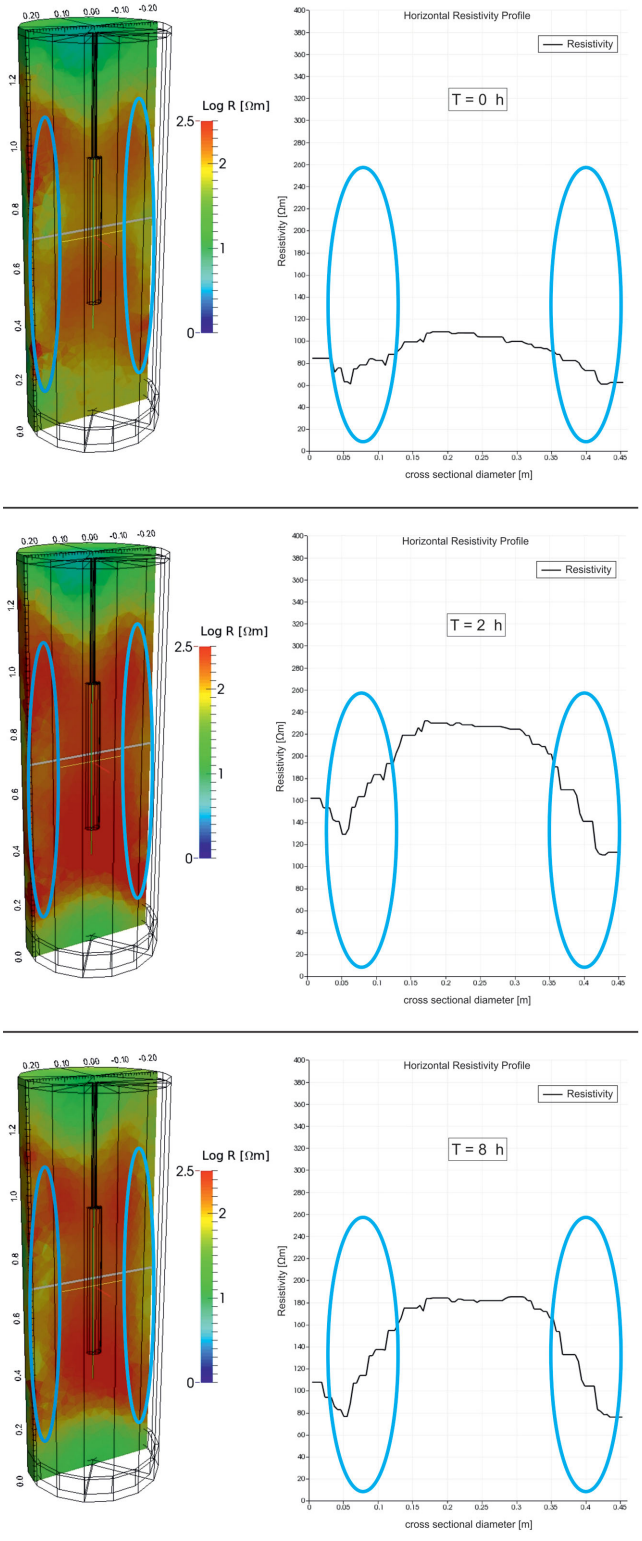

Figure 16. Horizontal resistivity profiles (grey line in left picture) for different states of hydrate dissociation. Top: initial resistivities before hydrate dissociation (only hydrate, no gas present). Middle: occurring hydrate dissociation. Emerging free gas phase increases resistivities along the profile (hydrate and gas present). Bottom: resistivities in the boundary region decrease again, indicating completed hydrate dissociation and advancing gas depletion (no hydrate, only gas present).

as the super saturated pore water entered the hydrate stability field in terms of *P–T* conditions. This leads to the conclusion that the residence time of dissolved methane in gas hydrate stability zones is short until it is consumed in hydrate formation.

Furthermore, we introduced a data processing routine which allowed the quantification of local changes of hydrate saturation and hydraulic permeability by measuring the electrical properties of the sediment sample. The spatial resistivity distribution obtained from the ERT data was converted into a quantitative spatial distribution of hydrate saturation by applying the Archie$_{var-phi}$ relation. The resulting information about the hydrate distribution can subsequently serve as input data for numerical simulations, for example, modelling production scenarios and history matching of experiments in LARS, or to adjust future dissociation experiments in LARS with respect to the obtained hydrate distribution.

The values of local hydrate saturation were used to estimate the local changes of hydraulic permeability within the sediment sample using the pore filling CK relation. The estimated permeability evolution yields helpful information in terms of understanding the changes of the sediment's hydraulic properties. Future plans involve additional experimental efforts to support the applied models with experimental permeability data.

During hydrate dissociation it could be shown that the gas and hydrate phases can qualitatively be monitored and tracked using ERT data. After setting the *P–T* conditions outside of the hydrate stability field, areas of increased electrical resistivity marked initialized hydrate decomposition, as the emerged free gas phase displaced remaining pore water of the respective areas. Supplemental temperature and pressure data allowed for advanced interpretation in terms of identifying areas of active hydrate dissociation as well as areas completely free of non-dissolved hydrocarbons.

The general alikeness of the data recorded during LARS RUNs 2 and 4 indicates that the results of our hydrate formation and dissociation experiments in LARS are reproducible.

ACKNOWLEDGEMENTS

The German Federal Ministry of Economy and Technology provided funding for this work within the SUGAR project through Research Grant 03SX250E.

Furthermore, the authors thank the staff of the GFZ workshops, Alexander Reichardt and Ronny Giese for invaluable technical help and for the construction of the ERT system.

REFERENCES

Archie, G.E., 1942. The electrical resistivity log as an aid in determining some reservoir characteristics, *Petroleum Transactions of AIME,* **146,** 54–62, doi:10.2118/942054-G.

Bauer, K., Haberland, C., Pratt, R., Hou, F., Mediali, B. & Weber, M., 2005. Ray-based cross-well tomography for P-wave velocity, anisotropy, and attenuation structure around the JAPEX/JNOC/GSC et al. Mallik 5L-38 gas hydrate production research well, *Geological Survey of Canada,* Bulletin 585, 21 p.

Buffett, B. & Zatsepina, O., 2000. Formation of gas hydrate from dissolved gas in natural porous media, *Mar. Geol.,* **164,** 69–77.

Carman, P., 1956. *Flow of Gases Through Porous Media,* Academic Press.

Dallimore, S.R. & Collett, T.S., 2005. Scientific results from the Mallik 2002 gas hydrate production research well program, Mackenzie Delta, Northwest Territories, Canada, *Geological Survey of Canada Ottawa,* Bulletin 585, doi:10.4095/220702.

Delli, M. & Grozic, J., 2013. Prediction Performance of Permeability Models in Gas-Hydrate-Bearing Sands, *SPE Journal, Society of Petroleum Engineers,* **18,** 274–284.

Ersland, G., Husebø, J., Graue, A. & Kvamme, B., 2009. Transport and storage of CO_2 in natural gas hydrate reservoirs, *Energy Procedia,* **1,** 3477–3484.

Garnett, J.C.M., 1904. Colours in metal glasses and in metallic films, *Phil. Trans. R. Soc. Lond., A.,* **203,** 385–420.

Günther, T., Rücker, C. & Spitzer, K., 2006. Three-dimensional modelling and inversion of dc resistivity data incorporating topography - II. Inversion, *Geophys. J. Int.,* **166,** 506–517.

Hazen, A., 1893. Some Physical Properties of Sands and Gravels with Special Reference to their Use in Filtration, *24th Annual Report, Massachusetts State Bureau of Health,* Publ. Doc. 34, 539–556.

Klauda, J.B. & Sandler, S.I., 2005. Global distribution of methane hydrate in ocean sediment, *Energy & Fuels,* **19,** 459–470.

Kleinberg, R.L., Flaum, C., Griffin, D.D., Brewer, P.G., Malby, G.E., Peltzer, E.T. & Yesinowski, J.P., 2003. Deep sea NMR: methane hydrate growth habit in porous media and its relationship to hydraulic permeability, deposit accumulation, and submarine slope stability, *J. geophys. Res.,* **108**(B10), 2508, doi:10.1029/2003JB002389.

Kneafsey, T.J., Tomutsa, L., Moridis, G.J., Seol, Y., Freifeld, B.M., Taylor, C.E. & Gupta, A., 2007. Methane hydrate formation and dissociation in a partially saturated core-scale sand sample, *Journal of Petroleum Science and Engineering,* **56,** 108–126.

Konno, Y. *et al.*, 2015. Permeability of sediment cores from methane hydrate deposit in the Eastern Nankai Trough, *Mar. Pet. Geol.,* doi:10.1016/j.marpetgeo.2015.02.020.

Kuhs, W.F. *et al.*, 2014. In-situ micro-structural studies of gas hydrate formation in sedimentary matrices, in *Proceedings of the 8th International Conference on Gas Hydrates ICGH 2014,* Beijing, China, pp. T1–122.

Kvenvolden, K.A. & Grantz, A., 1990. Gas hydrates of the Arctic Ocean region, in *The Geology of North America 50, The Arctic Ocean Region,* pp. 539–549, eds Grantz, A., Johnson, L. & Sweeney, J.F., Geological Society of America.

Landauer, R., 1952. The Electrical Resistance of Binary Metallic Mixtures, *J. Appl. Phys.,* **23,** 779–784.

Lee, W.S. & White, M., 2014. Guest molecule exchange kinetics for the 2012 Ignik Sikumi Gas Hydrate Field Trial, in *Offshore Technology Conference,* Houston, TX, USA.

Lichtenecker, K., 1926. Dielectric constant of artificial and natural mixtures, *Phys. Z,* **27,** 115–158.

Mavko, G., Mukerji, T. & Dvorkin, J.P., 2003. *The Rock Physics Handbook: Tools for Seismic Analysis of Porous Media,* Cambridge Univ. Press.

Milkov, A.V., Claypool, G.E., Lee, Y.-J. & Sassen, R., 2005. Gas hydrate systems at Hydrate Ridge offshore Oregon inferred from molecular and isotopic properties of hydrate-bound and void gases, *Geochim. Cosmochim. Acta,* **69,** 1007–1026.

Minagawa, H., Ohmura, R., Kamata, Y., Ebinuma, T., Narita, H. & Masuda, Y., 2005. Water permeability measurements of gas hydrate-bearing sediments, *Fifth International Conference on Gas Hydrates,* Trondheim, Norway, 1058.

Neustaedter, R., 1968. Log evaluation of deep Ellenburger gas zones, in *SPE Deep Drilling and Development Symposium,* Monahans, TX, USA.

Pearson, C.F., Halleck, P.M., McGuire, P.L., Hermes, R. & Mathews, M., 1983. Natural gas hydrate deposits: a review of in situ properties, *J. Phys. Chem.,* **87,** 4180–4185.

Priegnitz, M., Thaler, J., Spangenberg, E., Rücker, C. & Schicks, J.M., 2013. A cylindrical electrical resistivity tomography array for three-dimensional monitoring of hydrate formation and dissociation, *Rev. Sci. Instrum.,* **84,** 104502, doi:10.1063/1.4825372.

Rydzy, M.B., 2013. The effect of hydrate formation on the elastic properties of unconsolidated sediment, *PhD thesis,* Colorado School of Mines, Golden, CO.

Santamarina, J. *et al.*, 2015. Hydro-bio-geomechanical properties of hydrate-bearing sediments from Nankai Trough, *Mar. Pet. Geol.,* doi:10.1016/j.marpetgeo.2015.02.033.

Schicks, J.M., Spangenberg, E., Giese, R., Steinhauer, B., Klump, J. & Luzi, M., 2011. New approaches for the production of hydrocarbons from hydrate bearing sediments, *Energies,* **4,** 151–172.

Schicks, J.M., Spangenberg, E., Giese, R., Luzi-Helbing, M., Priegnitz, M. & Beeskow-Strauch, B., 2013. A counter-current heat-exchange reactor for the thermal stimulation of hydrate-bearing sediments, *Energies,* **6,** 3002–3016.

Schwalenberg, K., Haeckel, M., Poort, J. & Jegen, M., 2010. Evaluation of gas hydrate deposits in an active seep area using marine controlled source electromagnetics: results from Opouawe Bank, Hikurangi Margin, New Zealand, *Mar. Geol.,* **272,** 79–88.

Sen, P., Scala, C. & Cohen, M., 1981. A self-similar model for sedimentary rocks with application to the dielectric constant of fused glass beads, *Geophysics,* **46,** 781–795.

Sloan, E. & Koh, C., 2008. *Clathrate Hydrates of Natural Gases,* CRC Press.

Spangenberg, E., 2001. Modeling of the influence of gas hydrate content on the electrical properties of porous sediments, *J. geophys. Res.,* **106**(B4), 6535–6548.

Spangenberg, E. & Kulenkampff, J., 2006. Influence of methane hydrate content on electrical sediment properties, *Geophys. Res. Lett.,* **33,** L24315, doi:10.1029/2006GL028188.

Spangenberg, E., Priegnitz, M., Heeschen, K. & Schicks, J.M., 2015. Are Laboratory-Formed Hydrate-Bearing Systems Analogous to Those in Nature? *J. Chem. Eng. Data,* **60,** 258–268.

Stern, L.A., Kirby, S.H., Durham, W.B., Circone, S. & Waite, W.F., 2003. Laboratory synthesis of pure methane hydrate suitable for measurement of physical properties and decomposition behavior, in *Natural Gas Hydrate: Oceanic and Permafrost Environments,* pp. 323–348, ed. Max, M.D., Kluwer.

Terzaghi, K., 1955. *Influence of Geological Factors on the Engineering Properties of Sediments,* Harvard University.

Uddin, M., Wright, F. & Coombe, D., 2011. Numerical study of gas evolution and transport behaviours in natural gas-hydrate reservoirs, *J. Can. Pet. Technol.,* **50,** 70–88.

Von Stackelberg, M., Gotzen, O., Pietuchovsky, J., Wirtscher, O., Fruhbuss, H. & Meinhold, W., 1947. Struktur und Formel der Gashydrate, *Fortschr. der Mineralogie,* **26,** 122–124.

Waff, H.S., 1974. Theoretical considerations of electrical conductivity in a partially molten mantle and implications for geothermometry, *J. geophys. Res.,* **79,** 4003–4010.

Waite, W.F. & Spangenberg, E., 2013. Gas hydrate formation rates from dissolved-phase methane in porous laboratory specimens, *Geophys. Res. Lett.,* **40,** 4310–4315.

Wright, J.F., Uddin, M., Dallimore, S.R. & Coombe, D., 2011. Mechanisms of gas evolution and transport in a producing gas hydrate reservoir: an unconventional basis for successful history matching of observed production flow data, in *Proceedings of the 7th International Conference on Gas Hydrates ICGH 2011,* Edinburgh, Scotland.

Yamamoto, K., 2014. 2013 Methane hydrate offshore production test in the eastern Nankai Trough; a milestone on the path to real energy resource, in *Proceedings of the 8th International Conference on Gas Hydrates ICGH 2014,* Beijing, China, pp. T3–153.